Geophysical Research Letters

RESEARCH LETTER
10.1029/2019GL083084

Key Points:
- Uncertainty in the Atlantic Meridional Overturning Circulation is the main cause of the model spread in evolution of the warming pattern
- Warming in Northern Hemisphere extratropics tends to be surface trapped, leading to more positive lapse-rate and cloud feedbacks
- Models with stronger recovery in Atlantic Meridional Overturning Circulation tend to project a larger increase in net climate feedback

Supporting Information:
- Supporting Information S1

Correspondence to:
Y.-T. Hwang,
ythwang@ntu.edu.tw

Citation:
Lin, Y.-J., Hwang, Y.-T., Ceppi, P., & Gregory, J. M. (2019). Uncertainty in the Evolution of Climate Feedback Traced to the Strength of the Atlantic Meridional Overturning Circulation. *Geophysical Research Letters*, *46*, 12,331–12,339. https://doi.org/10.1029/2019GL083084

Received 30 MAR 2019
Accepted 9 OCT 2019
Accepted article online 22 OCT 2019
Published online 5 NOV 2019

Uncertainty in the Evolution of Climate Feedback Traced to the Strength of the Atlantic Meridional Overturning Circulation

Yuan-Jen Lin[1], Yen-Ting Hwang[1], Paulo Ceppi[2], and Jonathan M. Gregory[3,4]

[1]Department of Atmospheric Sciences, National Taiwan University, Taipei, Taiwan, [2]Grantham Institute, Imperial College London, London, UK, [3]NCAS-Climate, University of Reading, Reading, UK, [4]Met Office Hadley Centre, Exeter, UK

Abstract In most coupled climate models, effective climate sensitivity increases for a few decades following an abrupt CO_2 increase. The change in the climate feedback parameter between the first 20 years and the subsequent 130 years is highly model dependent. In this study, we suggest that the intermodel spread of changes in climate feedback can be partially traced to the evolution of the Atlantic Meridional Overturning Circulation. Models with stronger Atlantic Meridional Overturning Circulation recovery tend to project more amplified warming in the Northern Hemisphere a few decades after a quadrupling of CO_2. Tropospheric stability then decreases as the Northern Hemisphere gets warmer, which leads to an increase in both the lapse-rate and shortwave cloud feedbacks. Our results suggest that constraining future ocean circulation changes will be necessary for accurate climate sensitivity projections.

Plain Language Summary How much the Earth's climate will warm in response to increasing carbon dioxide concentration, a number known as climate sensitivity, is an essential metric of the impacts of anthropogenic climate change. Most current global climate models agree that the climate will become more sensitive as time passes, indicating an underestimation of future warming inferred from historical records. In this study, we report that the slow response of oceanic circulation has an influence on this time evolution of climate sensitivity. In the 15 state-of-the-art global climate models we investigate, the models projecting restrengthening of Atlantic Meridional Overturning Circulation after a few decades of weakening tend to simulate a more significant increase in climate sensitivity. We propose a mechanism as follows: Atlantic Meridional Overturning Circulation strengthening causes more enhanced surface warming in the Northern Hemisphere, altering the vertical stability of the global atmosphere. The changes in atmospheric vertical stability then strengthen the radiative feedbacks that amplify greenhouse gas forcing, accounting for the larger increase in climate sensitivity in these models. Our findings emphasize the important contribution of ocean circulation to the intermodel spread in climate change projections.

1. Introduction

Equilibrium climate sensitivity (ECS) refers to the globally averaged equilibrium surface air temperature response to an abrupt doubling of CO_2 concentration, and it has spanned a range of 1.5–4.5 K for decades (Charney et al., 1979; Flato et al., 2013). Since it takes thousands of years for coupled models to reach steady state, ECS is usually estimated by assuming the net climate feedback (λ) is time invariant (Gregory et al., 2004):

$$\mathrm{ECS} = -\frac{F}{\lambda}. \tag{1}$$

F is radiative forcing of $2\times CO_2$. The "constant λ" approximation has been applied to some atmospheric general circulation models coupled to slab ocean models, pointing out that the uncertainty in cloud feedback is the main cause of the intermodel spread of ECS (Bony et al., 2006). Many studies, however, have reported a time dependence of λ in atmosphere-ocean coupled general circulation models (AOGCMs), which adds another uncertainty in determining ECS (Armour, 2017; Block & Mauritsen, 2013; Geoffroy et al., 2013). The time dependence of λ has been related to the evolution of the surface warming pattern (Armour et al., 2013; Rose et al., 2014; Zhou et al., 2016).

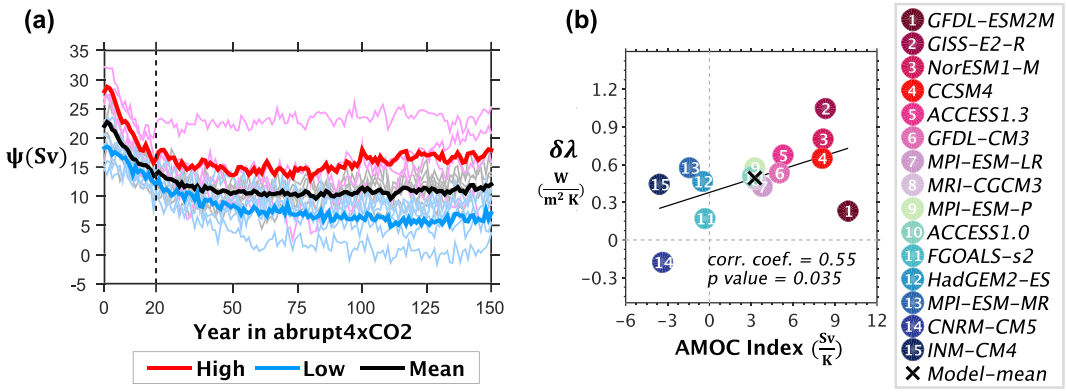

Figure 1. (a) The time evolution of Atlantic Meridional Overturning Circulation (AMOC) strength in abrupt4×CO_2 simulations. The strength at Year 0 is the 150-year mean in corresponding parallel piControl simulations. The black line indicates the multimodel mean, while the thick red (blue) line indicates the high (low) AMOC index composite mean, and the thin red (blue/gray) lines are from individual models with high (low/medium) AMOC index. (b) δλ versus the AMOC index. Each dot is one model, labeled in the box and colored according to the AMOC index.

How the surface warming pattern evolves under CO_2 forcing and how it varies among models are further issues to be confronted in narrowing the uncertainty of ECS. Many have argued for the importance of the ocean in controlling the surface warming pattern (Marshall et al., 2015; Winton et al., 2010, 2013). For example, Marshall et al. (2015) observed a broad correspondence in SST anomaly between the ocean-only model and multiple AOGCMs, especially the delayed warming in the North Atlantic and the Southern Ocean, suggesting that mechanisms controlling the SST response in coupled models are influenced by ocean processes.

To identify the mechanisms driving the distinct time evolution of climate feedbacks across AOGCMs, we diagnose the time-varying ocean processes, surface warming patterns, and climate feedbacks in fully coupled models (section 2). We show that part of the intermodel spread in climate feedback evolution can be traced to the evolution of the Atlantic Meridional Overturning Circulation (AMOC), via changes in the surface warming pattern and atmospheric stability (section 3). In section 4, we summarize our results and compare them with the previous studies focusing on the multimodel mean.

2. Materials and Methods

2.1. Model Data

We analyze the output from 15 climate models participating in the Coupled Model Intercomparison Project Phase 5 (CMIP5) that provide the required variables for our study (supporting information Table S1). The 150-year simulations with preindustrial conditions (piControl) and forced with an abrupt quadrupling of atmospheric CO_2 concentration (abrupt4×CO_2) are assessed. To remove any model drift, we calculate the anomalies by subtracting the piControl integration from the corresponding parallel abrupt4×CO_2 integration.

2.2. The Evolution of the Climate System per 1 K Global Warming

To represent the evolution of the climate system, we define an operator "δ" as follows:

$$\delta X = \left.\frac{dX}{d(GMT)}\right|_{Y21-150} - \left.\frac{dX}{d(GMT)}\right|_{Y1-20}. \quad (2)$$

X can be any of the target fields. Ordinary least-squares regression of annual-mean anomalies in X against annual- and global-mean surface air temperature anomaly (GMT) is separately done for the early (Years 1–20) and late (Years 21–150) periods. The separation at Year 20 approximately divides climate responses into fast and slow components (Geoffroy et al., 2013; Held et al., 2010). When X is surface air temperature (TAS), equation (2) gives the "surface warming pattern evolution" (δTAS; Figure 2a). When X is the global-mean net radiation at the top of atmosphere, the terms in equation (2) are the net climate feedback (λ) for the two time periods, and the difference gives the "net climate feedback evolution" (δλ). Different

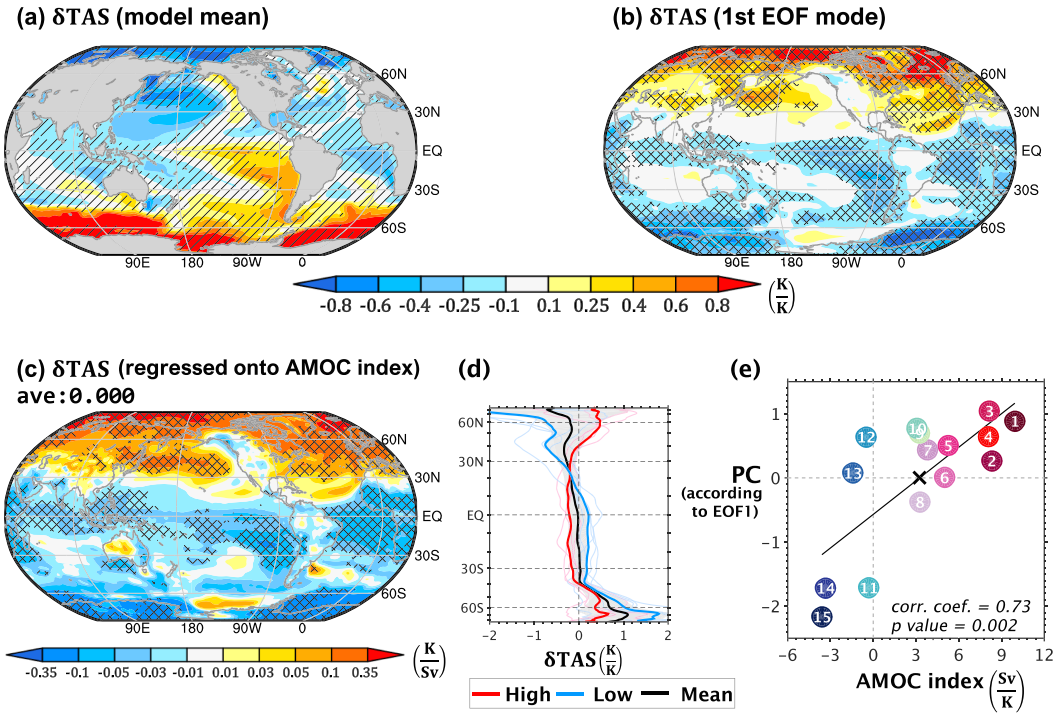

Figure 2. (a) Multimodel-mean pattern evolution of surface air temperature (δTAS). Hatching denotes an absolute multimodel mean <1 standard deviation across models. (b) The first empirical orthogonal function (EOF) pattern of δTAS across models. Statistical significance is assessed by regressing δTAS onto the principal component (PC) according to the first EOF. (c) The regression slopes of δTAS against the Atlantic Meridional Overturning Circulation (AMOC) index. (d) Zonally averaged δTAS. The meaning of colored lines is the same as in Figure 1a. The gray shading represents the multimodel mean ± 1 standard deviation (K/K) across models. Meshing in (b) and (c) denotes the significance at 95% confidence level. (e) The PC corresponding to the first EOF of δTAS versus the AMOC index.

choices of separation year have little influence on the magnitudes of δλ (Andrews et al., 2015). δλ can be further decomposed into various components using the radiative kernel method (Held & Shell, 2012; Pendergrass et al., 2018; Soden et al., 2008; see Text S1).

The terms in equation (2) are chosen to be derivatives with respect to GMT for two reasons (see Figure S1 for GMT evolution). First, the patterns of surface temperature and top-of-atmosphere radiation, expressed per unit of GMT increase, are generally assumed to be constant in a given model. This is an application of the common "pattern scaling" assumption. If pattern scaling holds exactly for X, equation (2) gives $\delta X = 0$; otherwise, δX measures the deviation from pattern scaling. Second, the change in any X tends to be larger for models which have greater ECS and hence greater GMT at all time. The use of the derivatives thus in effect normalizes δX with respect to ECS, removing that factor from the consideration of the spread among models in the projected changes.

2.3. AMOC index (δψ)

For each model, we first identify the AMOC strength (ψ) as the maximum of the ocean overturning mass stream function (variable name *msftmyz* or *msftyyz*) over the North Atlantic (north of 30°N), excluding the overturning shallower than 500 m (Gregory et al., 2005). We then define the "AMOC index (δψ)" as per equation (2) with X as the AMOC strength (ψ). The AMOC index quantifies the AMOC evolution from early to late periods in each model and is insensitive to the choice of separation year discussed in section 2.2 (Table S2). Variations in AMOC strength arising from natural variability tend to be substantially smaller than AMOC index values and are unlikely to explain the intermodel spread (see Text S2). With regard to our motivation for taking derivatives with respect to GMT (cf. the previous paragraph), there is no significant correlation of AMOC changes with ECS across models, so the second reason does not apply. The first reason is valid because it makes the early and late terms comparable, by normalizing responses with respect to the magnitude of climate change in the two periods.

3. Results

On average, in the 15 CMIP5 coupled climate models analyzed in this study, the climate system becomes more sensitive as it approaches equilibrium, with the multimodel-mean net climate feedback (λ) evolving from -1.37 Wm^{-2} K^{-1} during the first 20 years of abrupt4×CO_2 simulations to -0.87 Wm^{-2} K^{-1} during the following 130 years. The difference in multimodel-mean λ (0.50 Wm^{-2} K^{-1}) between the periods is consistent with previous studies (Andrews et al., 2015; Ceppi & Gregory, 2017). At the same time, this time evolution of climate feedback ($\delta\lambda$) is highly model dependent, ranging from -0.18 to 1.05 Wm^{-2} K^{-1} across models, a range 2.5 times as large as the magnitude of their multimodel mean.

To identify the root cause of the intermodel spread of climate feedback evolution, we investigate the evolution of global meridional overturning circulation, quantified as the meridional mass stream function for the global ocean (Manabe & Stouffer, 1993; Talley et al., 2003). An empirical orthogonal function (EOF) analysis (also known as principal component analysis) of global meridional overturning circulation evolution, applied across models, shows that the AMOC evolution is the main uncertainty of the global ocean circulation response (see Text S3). This is consistent with previous studies highlighting the uncertainty in AMOC projections in CMIP5 models (Cheng et al., 2013; Heuzé et al., 2015; Wang et al., 2014). Based on the AMOC evolution, the 15 CMIP5 models can be classified into three groups, with high, medium, and low AMOC indices ($\delta\psi$; see Figure S2 for the list of models in each composite). In the high AMOC index composite, the AMOC slows down significantly in the initial stage of warming but recovers in strength in the later stage; by contrast, in the low AMOC index composite, the AMOC slows down moderately in the initial warming but continues slowing down as warming proceeds (Figure 1a). It is possible that models in the low index group would eventually project AMOC restrengthening if the lengths of the simulations were extended. The timing of the restrengthening could be more than a thousand years after quadrupling CO_2 (Li et al., 2013; Stouffer & Manabe, 2003). The weakening of the AMOC in response to greenhouse gas forcing is predominantly due to the buoyancy effect of changes in surface heat flux, with the effect of changes in surface water flux being relatively minor (Gregory et al., 2005; Gregory et al., 2016). However, substantially increased meltwater from the Greenland ice sheet, not included in CMIP5 experiments, could further weaken the AMOC (Saenko et al., 2017; Sgubin et al., 2015; Stouffer et al., 2006; Swingedouw et al., 2009, 2015).

The cause of the intermodel spread in AMOC evolution is beyond the scope of this study. Instead, we report that the spread in the AMOC evolution can partly contribute to the intermodel spread in net climate feedback evolution ($\delta\lambda$). $\delta\lambda$ is positively correlated with the AMOC index ($\delta\psi$; $r = 0.55$; Figure 1b). In the rest of the paper, we will explain why models with higher AMOC index tend to project a larger increase in λ through changes in surface warming pattern and tropospheric stability.

3.1. The Uncertainty in the Surface Warming Pattern Evolution (δTAS)

As the climate system approaches equilibrium, the multimodel-mean surface warming pattern becomes less pronounced over the Arctic region and the western North Pacific and more pronounced over the tropical East Pacific and the Southern Ocean (Figure 2a), consistent with Andrews et al. (2015) and Ceppi and Gregory (2017). In most regions over the globe, we note that the evolution of the surface warming pattern (δTAS) is quite model dependent, since the magnitudes of 1 standard deviation of δTAS across models are larger than the multimodel-mean δTAS. In addition, the first EOF of δTAS across models, explaining 48% of the total variance, exhibits a difference between the Northern and Southern Hemispheres (NH and SH; Figure 2b), suggesting that the degree of hemispheric asymmetry is the main uncertainty in the evolution of the surface warming pattern.

We propose that the intermodel spread of the AMOC evolution is a cause of the spread in δTAS. To visualize the spatial pattern of the AMOC-related δTAS spread, Figure 2c shows the regression slopes of δTAS against the AMOC index. Models with higher AMOC index tend to project increasingly pronounced warming in the NH extratropics and increasingly weak warming in the tropics and SH as time passes and vice versa for models with lower AMOC index (Figures 2c and 2d). Note the remarkable similarity between the AMOC-related spread of δTAS (Figure 2c) and the first EOF of δTAS (Figure 2b; area-weighted pattern correlation = 0.94). Also, the AMOC index is well correlated with the principal component corresponding to the first EOF (Figure 2e). We therefore suggest that the varying AMOC evolution is the main cause for the uncertainties

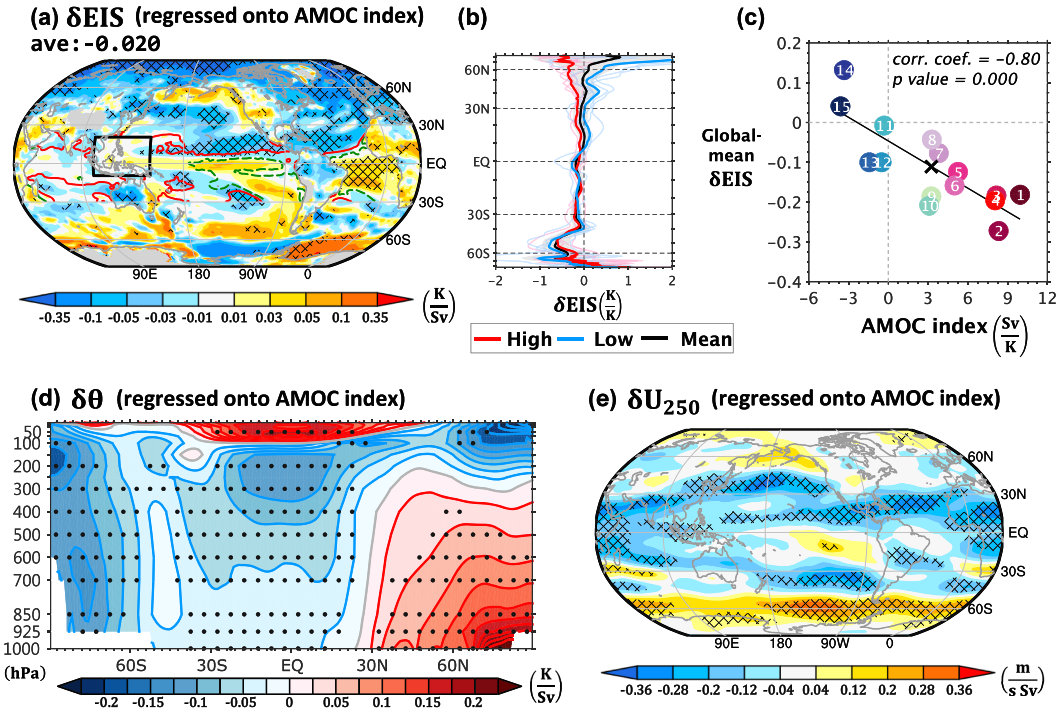

Figure 3. The regression slopes of (a) estimated inversion strength (EIS) evolution (δEIS), (d) zonal-mean potential temperature evolution (δθ), and (e) 250-hPa zonal wind evolution (δU_{250}) against the Atlantic Meridional Overturning Circulation (AMOC) index. Stippling and meshing denote the significance at 95% confidence level. Contours in (a) denote the anomalous δTAS relative to the warm pool (black box), with solid red (dashed green) indicating a more positive (negative) δTAS. This is done only in the tropics. (b) Zonally averaged δEIS. The meaning of colored lines and shading is the same as in Figure 2d. (c) Global-mean δEIS versus the AMOC index.

in the warming pattern evolution (δTAS). Previous studies have attributed the surface temperature response on decadal and longer time scales to the strength of the deep ocean circulation, based on results from a single model or from the CMIP5 multimodel-mean (Marshall et al., 2015; Trossman et al., 2016). Here we corroborate that attribution by relating the intermodel spread of the surface warming pattern evolution to the varying AMOC evolution among models.

3.2. The Uncertainty in the Tropospheric Stability Evolution (δEIS)

Varying hemispheric asymmetry in the surface warming pattern evolution can lead to uncertainty in the tropospheric stability response, shown to be a key mechanism for the time evolution of climate feedbacks (Andrews & Webb, 2018; Ceppi & Gregory, 2017). Here we quantify tropospheric stability by calculating the estimated inversion strength (EIS), defined as the difference in potential temperature between 700 hPa and the surface, corrected to account for the dependence of the moist adiabat on mean temperature (Wood & Bretherton, 2006). In general, the multimodel-mean EIS evolution (δEIS, defined using equation (2)) has the opposite sign from the multimodel-mean warming pattern evolution (δTAS; Figure S3, consistent with Figure 1b in Ceppi & Gregory, 2017). Also, similar to δTAS, δEIS appears to be model dependent. For example, in the Arctic, the North Atlantic, and the western North Pacific, the negative regression slopes indicate that models with stronger AMOC recovery (high AMOC index) tend to project an increasingly unstable troposphere in these regions and vice versa for the positive regression slopes in the tropical South Atlantic (Figure 3a). Dominated by the negative correlation in the NH, Figure 3c shows that the global-mean EIS evolution negatively correlates with the AMOC index.

Our interpretation for the link between hemispherically asymmetric warming pattern and global EIS response is as follows. The pronounced warming in the relatively stable NH extratropics tends to remain trapped near the surface, resulting in a more unstable troposphere. The warming is increasingly pronounced if the AMOC index is higher, accounting for the negative regression slopes of δEIS against the AMOC index. In the tropics, consistent with the weak temperature gradient approximation (Sobel et al., 2002), the

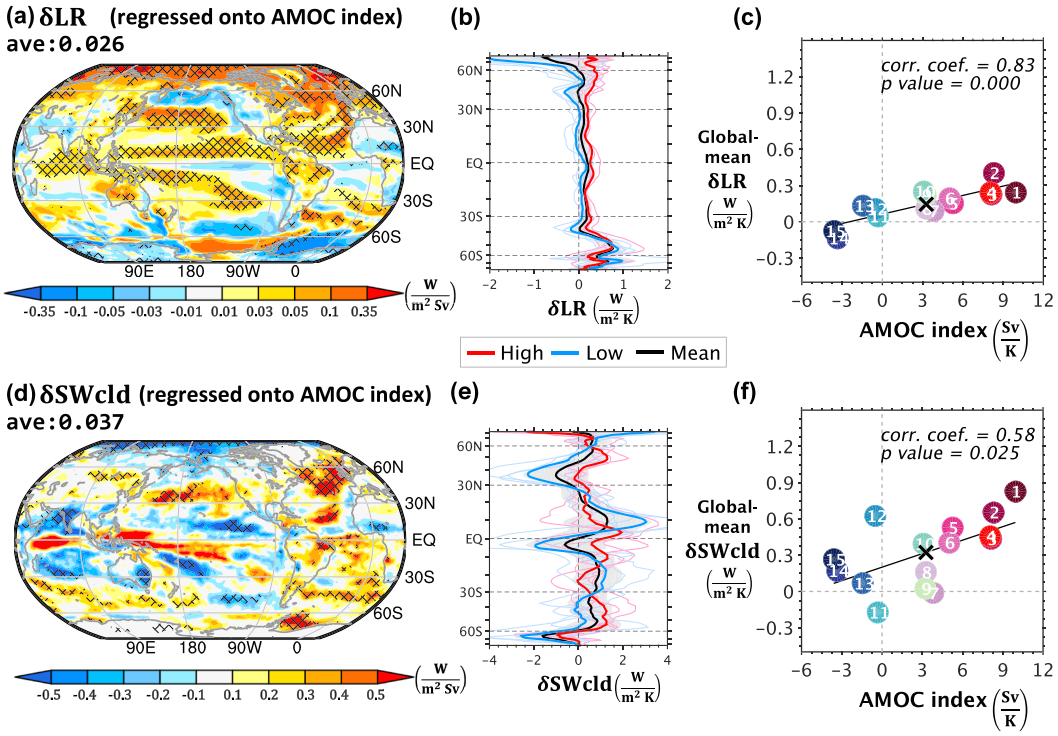

Figure 4. (a) The regression slopes of lapse-rate feedback evolution (δLR) against the Atlantic Meridional Overturning Circulation (AMOC) index, with meshing denoting the significance at 95% confidence level. (b) Zonally averaged δLR. The meaning of colored lines and shading is the same as in Figure 2d. (c) The global-mean δLR versus the AMOC index. (d–f) Same as (a)–(c) but for shortwave cloud feedback evolution (δSWcld).

temperature of the free troposphere is uniform and is determined by the SST over the deep convective regions (e.g., the West Pacific warm pool), where the lapse rate is close to a moist adiabat. The regression slopes of δTAS against the AMOC index are negative in the West Pacific warm pool (Figure 2c). The approximation explains a larger decrease in temperature of the free troposphere throughout the entire tropics for models with higher AMOC index (not shown). Therefore, regions with positive or insignificant regression slopes of δTAS against AMOC index exhibit negative regression slopes of δEIS. Consistently, Figure 3a shows that regions with more positive δTAS relative to the warm pool (red contours) would project more negative δEIS and vice versa for the regions with more negative δTAS relative to the warm pool (green contours). An exception to this behavior is in the SH extratropics, where the suppressed warming response over Antarctica is not trapped near the surface as in the NH extratropics. Instead, it is vertically uniform and can be ascribed to a more positive southern hemisphere annular mode. A more positive southern hemisphere annular mode is characterized by the band of westerly winds contracting toward Antarctica (Figure 3e) and is associated with equivalent barotropic wind and temperature anomalies (Thompson & Wallace, 2000).

3.3. The Uncertainty in the Climate Feedback Evolution (δλ)

The AMOC-related spread in global EIS evolution affects the lapse-rate feedback. Figure 4a shows the regression slopes of lapse-rate feedback evolution against the AMOC index, which is strongly anticorrelated with the regression slopes of the EIS evolution (Figure 3a; area-weighted pattern correlation = −0.92). In the Arctic, the North Atlantic, and most of the North Pacific, the troposphere becomes more unstable in the models with higher AMOC index. A more unstable troposphere indicates a reduced cooling ability of the free troposphere, which then results in a more positive lapse-rate feedback. Since models with a more positive AMOC index tend to project a larger decrease in global-mean EIS (Figure 3c), those models should also feature a larger increase in global-mean lapse-rate feedback. Indeed, Figure 4c shows a positive correlation (r = 0.83) between the AMOC index and the global-mean change in lapse-rate feedback. In summary, models with a higher AMOC index tend to project a stronger decrease in the NH tropospheric stability while

having little influence on the vertical temperature profile in the SH. This hemispherically asymmetric amplitude of stability response to the varying AMOC evolution results in global-mean changes in EIS and lapse-rate feedback against the AMOC index.

Meanwhile, the EIS evolution also contributes to the evolution of shortwave cloud feedback in specific regions. Figure 4d shows that shortwave cloud feedback becomes more positive in the North Atlantic and the North Pacific midlatitudes, where δEIS is negative. The destabilization of the lower troposphere acts to reduce low cloud cover, which leads to a more positive shortwave cloud feedback, associated with a higher AMOC index. In the tropics, the degree of Intertropical Convergence Zone (ITCZ) shift affects the shortwave cloud feedback. Consistent with the energetic framework (Friedman et al., 2013; Kang et al., 2008, 2009), models with higher AMOC index, tending to project NH warming, produce a weaker southward ITCZ shift (Figure S4), which results in a more negative (positive) shortwave cloud feedback in the north (south; Figures 4d and 4e). With positive and negative values generally cancelling out, the AMOC-related spread in tropical mean shortwave cloud feedback evolution contributes little to the global-mean change. Instead, it is the spread in the NH midlatitudes that largely makes up the positive correlation between the AMOC index and the global-mean change in shortwave cloud feedback (Figure 4f). While some of the spread in shortwave cloud feedback is compensated by the spread in longwave cloud feedback, we note that this compensation mostly happens in the tropics (Figure S5g). In the extratropics, the change in net cloud feedback is dominated by the shortwave component (Figure S5j). Thus, the mechanism described above may explain the positive correlation between the AMOC index and the area-averaged net cloud feedback evolution poleward of 30° ($r = 0.61$). Apart from the influence of tropospheric stability mentioned here, we note that the intermodel spread of cloud feedback could arise from a dependence on parameterization and resolution (Vial et al., 2013; Webb et al., 2015).

In addition to lapse-rate and cloud feedbacks, the AMOC evolution also has an impact on other feedback components. In models with stronger AMOC recovery, for example, albedo feedback becomes more positive in the NH polar region due to more melting ice, where the enhanced warming occurs, and vice versa for the SH polar region with smaller magnitudes (Figure S5a). Similar to longwave cloud feedback, the relative humidity feedback evolves toward more positive (negative) values in the NH (SH) tropics, indicating a northward shift of the ITCZ (Figure S5d). While the varying AMOC evolution influences the pattern evolution of these two feedbacks, the correlations between the AMOC index and the global-mean changes in relative humidity and surface albedo feedbacks are not significant (Figures S5c and S5f). Also, we note that the relationship between the AMOC index and the changes in most of the climate feedback components cannot be explained if assuming time-invariant local feedbacks (Armour et al., 2013). Instead, the evolution of tropospheric stability introduces nonlinearity in local climate feedbacks (Zhou et al., 2016; Ceppi & Gregory, 2017; see Text S4).

4. Summary and Discussion

In this study, we suggest that the intermodel spread in net climate feedback evolution (δλ) can be partially traced to the evolution of the AMOC strength. Models with stronger AMOC recovery tend to project a larger increase in net climate feedback, indicating more sensitive climate over longer time scales. The interpretation for the link between the AMOC evolution and the feedback change is as follows: The strengthening of AMOC over long time scales shifts the location of warming to NH extratropical regions, leading to a global destabilization of the troposphere and resulting in more positive lapse rate and shortwave cloud feedbacks. Similar relationships between AMOC strength and radiative anomalies are also found in decadal-scale unforced variability in the piControl simulations (see Text S5).

Interestingly, our interpretation that warmer NH leads to more sensitive climate cannot be applied to understanding the evolution of the multimodel-mean climate feedback. For the multimodel mean, the increase in λ is accompanied by enhanced warming mostly in the SH, especially in the tropical Southeast Pacific and the Southern Ocean (Figure 2a). In our analysis of the intermodel spread, the warming pattern evolution among models includes varying degrees of the north-south contrast (Figure 2b), which contributes to the intermodel spread of the global EIS response and the climate feedback evolution.

The dependence of climate feedbacks on the surface warming pattern has been an active research area. Some studies have focused on the east-west contrast of the surface warming pattern (Andrews & Webb, 2018;

Ceppi & Gregory, 2017; Zhou et al., 2017); for example, Zhou et al. (2017) suggest that the cloud feedback is more negative in response to western Pacific warming and more positive in response to warming in the eastern Pacific. On the other hand, others emphasize the tropics-extratropics contrast, suggesting that the climate will become more sensitive as the ocean heat uptake pattern evolves (Liu, Lu, Garuba, Huang, et al., 2018; Liu, Lu, Garuba, Leung, et al., 2018; Rose et al., 2014; Rugenstein et al., 2016). By investigating the cause of intermodel spread in the time dependence of climate feedbacks, we identify an additional geographical structure for controlling global-mean climate feedbacks: The variation of SST in the more stable NH high latitudes tends to be more confined in the lower troposphere than the variation of SST in the SH counterparts and is more likely to trigger positive radiative feedbacks. In future work, idealized experiments will be needed to provide a full understanding of the influence of SST patterns on climate feedbacks.

Acknowledgments
We thank three anonymous reviewers for constructive comments and A. Pendergrass for providing radiative kernels (https://doi.org/10.5281/zenodo.997899). We acknowledge the World Climate Research Programme's Working Group on Coupled Modelling, which is responsible for CMIP, and we thank the climate modeling groups (listed in Table S1) for producing and making available their model output. For CMIP, the U.S. DOE's Program for Climate Model Diagnosis and Intercomparison provided coordinating support and led development of software infrastructure in partnership with the Global Organization for Earth System Science Portals. Data related to this work are products of CMIP5 simulations, which can be downloaded from https://esgf-node.llnl.gov/search/cmip5/. Y. J. L. and Y. T. H. were supported by Ministry of Science and Technology of Taiwan (MOST 107-2636-M-002-001 and MOST 108-2636-M-002-007-). P. C. is supported by an Imperial College Research Fellowship. J. M. G. was supported by the European Research Council under the European Union's Horizon 2020 research and innovation programme (Grant agreement 786427, project "Couplet").

References

Andrews, T., Gregory, J. M., & Webb, M. J. (2015). The dependence of radiative forcing and feedback on evolving patterns of surface temperature change in climate models. *Journal of Climate*, *28*(4), 1630–1648. https://doi.org/10.1175/Jcli-D-14-00545.1

Andrews, T., & Webb, M. J. (2018). The dependence of global cloud and lapse rate feedbacks on the spatial structure of tropical Pacific warming. *Journal of Climate*, *31*(2), 641–654. https://doi.org/10.1175/JCLI-D-17-0087.1

Armour, K. C. (2017). Energy budget constraints on climate sensitivity in light of inconstant climate feedbacks. *Nature Climate Change*, *7*(5), 331–335. https://doi.org/10.1038/nclimate3278

Armour, K. C., Bitz, C. M., & Roe, G. H. (2013). Time-varying climate sensitivity from regional feedbacks. *Journal of Climate*, *26*(13), 4518–4534. https://doi.org/10.1175/JCLI-D-12-00544.1

Block, K., & Mauritsen, T. (2013). Forcing and feedback in the MPI-ESM-LR coupled model under abruptly quadrupled CO_2. *Journal of Advances in Modeling Earth Systems*, *5*, 676–691. https://doi.org/10.1002/jame.20041

Bony, S., Colman, R., Kattsov, V. M., Allan, R. P., Bretherton, C. S., Dufresne, J.-L., et al. (2006). How well do we understand and evaluate climate change feedback processes? *Journal of Climate*, *19*(15), 3445–3482. https://doi.org/10.1175/JCLI3819.1

Ceppi, P., & Gregory, J. M. (2017). Relationship of tropospheric stability to climate sensitivity and Earth's observed radiation budget. *Proceedings of the National Academy of Sciences*, *114*(50), 13,126–13,131. https://doi.org/10.1073/pnas.1714308114

Charney, J. G., Arakawa, A., Baker, D. J., Bolin, B., Dickinson, R. E., Goody, R. M., et al. (1979). *Carbon dioxide and climate: A scientific assessment*. Washington, DC: National Academy of Sciences.

Cheng, W., Chiang, J. C. H., & Zhang, D. X. (2013). Atlantic Meridional Overturning Circulation (AMOC) in CMIP5 models: RCP and historical simulations. *Journal of Climate*, *26*(18), 7187–7197. https://doi.org/10.1175/Jcli-D-12-00496.1

Flato, G., Marotzke, J., Abiodun, B., Braconnot, P., Chou, S. C., Collins, W., et al. (2013). Evaluation of climate models. In T. F. Stocker, D. Qin, G.-K. Plattner, M. Tignor, S. K. Allen, J. Boschung, A. Nauels, Y. Xia, V. Bex, & P. M. Midgley (Eds.), *Climate change 2013: The physical science basis. Contribution of Working Group I to the Fifth Assessment Report of the Intergovernmental Panel on Climate Change*, (pp. 741–866). Cambridge, United Kingdom and New York, NY, USA: Cambridge University Press.

Friedman, A. R., Hwang, Y.-T., Chiang, J. C., & Frierson, D. M. (2013). Interhemispheric temperature asymmetry over the twentieth century and in future projections. *Journal of Climate*, *26*(15), 5419–5433. https://doi.org/10.1175/JCLI-D-12-00525.1

Geoffroy, O., Saint-Martin, D., Bellon, G., Voldoire, A., Olivié, D., & Tytéca, S. (2013). Transient climate response in a two-layer energy-balance model. Part II: Representation of the efficacy of deep-ocean heat uptake and validation for CMIP5 AOGCMs. *Journal of Climate*, *26*(6), 1859–1876. https://doi.org/10.1175/JCLI-D-12-00196.1

Gregory, J., Dixon, K., Stouffer, R., Weaver, A., Driesschaert, E., Eby, M., et al. (2005). A model intercomparison of changes in the Atlantic thermohaline circulation in response to increasing atmospheric CO_2 concentration. *Geophysical Research Letters*, *32*, L12703. https://doi.org/10.1029/2005GL023209

Gregory, J., Ingram, W., Palmer, M., Jones, G., Stott, P., Thorpe, R., et al. (2004). A new method for diagnosing radiative forcing and climate sensitivity. *Geophysical Research Letters*, *31*, L03205. https://doi.org/10.1029/2003GL018747

Gregory, J. M., Bouttes, N., Griffies, S. M., Haak, H., Hurlin, W. J., Jungclaus, J., et al. (2016). The Flux-Anomaly-Forced Model Intercomparison Project (FAFMIP) contribution to CMIP6: Investigation of sea-level and ocean climate change in response to CO forcing. *Geoscientific Model Development*, *9*(11), 3993–4017. https://doi.org/10.5194/gmd-9-3993-2016

Held, I. M., & Shell, K. M. (2012). Using relative humidity as a state variable in climate feedback analysis. *Journal of Climate*, *25*(8), 2578–2582. https://doi.org/10.1175/Jcli-D-11-00721.1

Held, I. M., Winton, M., Takahashi, K., Delworth, T., Zeng, F., & Vallis, G. K. (2010). Probing the fast and slow components of global warming by returning abruptly to preindustrial forcing. *Journal of Climate*, *23*(9), 2418–2427. https://doi.org/10.1175/2009JCLI3466.1

Heuzé, C., Heywood, K. J., Stevens, D. P., & Ridley, J. K. (2015). Changes in global ocean bottom properties and volume transports in CMIP5 models under climate change scenarios. *Journal of Climate*, *28*(8), 2917–2944. https://doi.org/10.1175/JCLI-D-14-00381.1

Kang, S. M., Frierson, D. M., & Held, I. M. (2009). The tropical response to extratropical thermal forcing in an idealized GCM: The importance of radiative feedbacks and convective parameterization. *Journal of the Atmospheric Sciences*, *66*(9), 2812–2827. https://doi.org/10.1175/2009JAS2924.1

Kang, S. M., Held, I. M., Frierson, D. M., & Zhao, M. (2008). The response of the ITCZ to extratropical thermal forcing: Idealized slab-ocean experiments with a GCM. *Journal of Climate*, *21*(14), 3521–3532. https://doi.org/10.1175/2007JCLI2146.1

Li, C., von Storch, J.-S., & Marotzke, J. (2013). Deep-ocean heat uptake and equilibrium climate response. *Climate Dynamics*, *40*(5-6), 1071–1086. https://doi.org/10.1007/s00382-012-1350-z

Liu, F., Lu, J., Garuba, O., Leung, L. R., Luo, Y., & Wan, X. (2018). Sensitivity of surface temperature to oceanic forcing via q-flux Green's function experiments. Part I: Linear response function. *Journal of Climate*, *31*(9), 3625–3641. https://doi.org/10.1175/JCLI-D-17-0462.1

Liu, F., Lu, J., Garuba, O. A., Huang, Y., Leung, L. R., Harrop, B. E., & Luo, Y. (2018). Sensitivity of surface temperature to oceanic forcing via q-flux Green's function experiments. Part II: Feedback decomposition and polar amplification. *Journal of Climate*, *31*(17), 6745–6761. https://doi.org/10.1175/JCLI-D-18-0042.1

Manabe, S., & Stouffer, R. J. (1993). Century-scale effects of increased atmospheric CO_2 on the ocean–atmosphere system. *Nature*, *364*(6434), 215–218. https://doi.org/10.1038/364215a0

Marshall, J., Scott, J. R., Armour, K. C., Campin, J. M., Kelley, M., & Romanou, A. (2015). The ocean's role in the transient response of climate to abrupt greenhouse gas forcing. *Climate Dynamics*, *44*(7-8), 2287–2299. https://doi.org/10.1007/s00382-014-2308-0

Pendergrass, A. G., Conley, A., & Vitt, F. M. (2018). Surface and top-of-atmosphere radiative feedback kernels for CESM-CAM5. *Earth System Science Data*, *10*(1), 317–324. https://doi.org/10.5194/essd-10-317-2018

Rose, B. E. J., Armour, K. C., Battisti, D. S., Feldl, N., & Koll, D. D. B. (2014). The dependence of transient climate sensitivity and radiative feedbacks on the spatial pattern of ocean heat uptake. *Geophysical Research Letters*, *41*, 1071–1078. https://doi.org/10.1002/2013gl058955

Rugenstein, M. A. A., Caldeira, K., & Knutti, R. (2016). Dependence of global radiative feedbacks on evolving patterns of surface heat fluxes. *Geophysical Research Letters*, *43*, 9877–9885. https://doi.org/10.1002/2016gl070907

Saenko, O. A., Yang, D., & Myers, P. G. (2017). Response of the North Atlantic dynamic sea level and circulation to Greenland meltwater and climate change in an eddy-permitting ocean model. *Climate Dynamics*, *49*(7-8), 2895–2910. https://doi.org/10.1007/s00382-016-3495-7

Sgubin, G., Swingedouw, D., Drijfhout, S., Hagemann, S., & Robertson, E. (2015). Multimodel analysis on the response of the AMOC under an increase of radiative forcing and its symmetrical reversal. *Climate Dynamics*, *45*(5-6), 1429–1450. https://doi.org/10.1007/s00382-014-2391-2

Sobel, A. H., Held, I. M., & Bretherton, C. S. (2002). The ENSO signal in tropical tropospheric temperature. *Journal of Climate*, *15*(18), 2702–2706. https://doi.org/10.1175/1520-0442(2002)015<2702:TESITT>2.0.CO;2

Soden, B. J., Held, I. M., Colman, R., Shell, K. M., Kiehl, J. T., & Shields, C. A. (2008). Quantifying climate feedbacks using radiative kernels. *Journal of Climate*, *21*(14), 3504–3520. https://doi.org/10.1175/2007JCLI2110.1

Stouffer, R., & Manabe, S. (2003). Equilibrium response of thermohaline circulation to large changes in atmospheric CO_2 concentration. *Climate Dynamics*, *20*(7-8), 759–773. https://doi.org/10.1007/s00382-002-0302-4

Stouffer, R. J., Yin, J., Gregory, J., Dixon, K., Spelman, M., Hurlin, W., et al. (2006). Investigating the causes of the response of the thermohaline circulation to past and future climate changes. *Journal of Climate*, *19*(8), 1365–1387. https://doi.org/10.1175/JCLI3689.1

Swingedouw, D., Mignot, J., Braconnot, P., Mosquet, E., Kageyama, M., & Alkama, R. (2009). Impact of freshwater release in the North Atlantic under different climate conditions in an OAGCM. *Journal of Climate*, *22*(23), 6377–6403. https://doi.org/10.1175/2009JCLI3028.1

Swingedouw, D., Rodehacke, C. B., Olsen, S. M., Menary, M., Gao, Y., Mikolajewicz, U., & Mignot, J. (2015). On the reduced sensitivity of the Atlantic overturning to Greenland ice sheet melting in projections: A multi-model assessment. *Climate Dynamics*, *44*(11-12), 3261–3279. https://doi.org/10.1007/s00382-014-2270-x

Talley, L. D., Reid, J. L., & Robbins, P. E. (2003). Data-based meridional overturning streamfunctions for the global ocean. *Journal of Climate*, *16*(19), 3213–3226. https://doi.org/10.1175/1520-0442(2003)016<3213:DMOSFT>2.0.CO;2

Thompson, D. W., & Wallace, J. M. (2000). Annular modes in the extratropical circulation. Part I: Month-to-month variability. *Journal of Climate*, *13*(5), 1000–1016. https://doi.org/10.1175/1520-0442(2000)013<1000:AMITEC>2.0.CO;2

Trossman, D., Palter, J., Merlis, T., Huang, Y., & Xia, Y. (2016). Large-scale ocean circulation-cloud interactions reduce the pace of transient climate change. *Geophysical Research Letters*, *43*, 3935–3943. https://doi.org/10.1002/2016GL067931

Vial, J., Dufresne, J.-L., & Bony, S. (2013). On the interpretation of inter-model spread in CMIP5 climate sensitivity estimates. *Climate Dynamics*, *41*(11-12), 3339–3362. https://doi.org/10.1007/s00382-013-1725-9

Wang, C. Z., Zhang, L. P., Lee, S. K., Wu, L. X., & Mechoso, C. R. (2014). A global perspective on CMIP5 climate model biases. *Nature Climate Change*, *4*(3), 201–205. https://doi.org/10.1038/Nclimate2118

Webb, M. J., Lock, A. P., Bretherton, C. S., Bony, S., Cole, J. N., Idelkadi, A., et al. (2015). The impact of parametrized convection on cloud feedback. *Philosophical Transactions of the Royal Society A: Mathematical, Physical and Engineering Sciences*, *373*, 20140414. https://doi.org/10.1098/rsta.2014.0414

Winton, M., Griffies, S. M., Samuels, B. L., Sarmiento, J. L., & Frölicher, T. L. (2013). Connecting changing ocean circulation with changing climate. *Journal of Climate*, *26*(7), 2268–2278. https://doi.org/10.1175/JCLI-D-12-00296.1

Winton, M., Takahashi, K., & Held, I. M. (2010). Importance of ocean heat uptake efficacy to transient climate change. *Journal of Climate*, *23*(9), 2333–2344. https://doi.org/10.1175/2009jcli3139.1

Wood, R., & Bretherton, C. S. (2006). On the relationship between stratiform low cloud cover and lower-tropospheric stability. *Journal of Climate*, *19*(24), 6425–6432. https://doi.org/10.1175/JCLI3988.1

Zhou, C., Zelinka, M. D., & Klein, S. A. (2016). Impact of decadal cloud variations on the Earth's energy budget. *Nature Geoscience*, *9*(12), 871–874. https://doi.org/10.1038/ngeo2828

Zhou, C., Zelinka, M. D., & Klein, S. A. (2017). Analyzing the dependence of global cloud feedback on the spatial pattern of sea surface temperature change with a Green's function approach. *Journal of Advances in Modeling Earth Systems*, *9*, 2174–2189. https://doi.org/10.1002/2017MS001096

GEOPHYSICAL RESEARCH LETTER

Supporting Information for

Uncertainty in the evolution of climate feedback traced to the strength of the Atlantic Meridional Overturning Circulation

Yuan-Jen Lin[1], Yen-Ting Hwang[1]†, Paulo Ceppi[2], and Jonathan Gregory[3,4]

[1]Department of Atmospheric Sciences, National Taiwan University, Taiwan

[2]Grantham Institute, Imperial College London, United Kingdom

[3]NCAS-Climate, University of Reading, Reading, United Kingdom

[4]Met Office Hadley Centre, Exeter, United Kingdom

†Corresponding author: Yen-Ting Hwang (ythwang@ntu.edu.tw)

Contents of this file

Text S1. Climate feedback decomposition

As mentioned in Section 2.2, the evolution of climate feedback, $\delta\lambda$, can be further decomposed into various components. We use radiative kernels to decompose changes in TOA radiation into the contributions of changes in temperature, water vapor, surface albedo, and clouds in each month (Soden et al., 2008). Radiative kernels are calculated with the Community Atmospheric Model version 5 (CAM5) (Pendergrass et al., 2018). Changes in water vapor can be further divided into two components; (1) changes assuming constant relative humidity, and (2) changes in relative humidity. Here we include the first component in the temperature feedbacks (Held & Shell, 2012). Changes in cloud-radiative effects, which are known to contain non-cloud effects, can also be adjusted using radiative kernels to estimate cloud feedback (Soden et al., 2008).

Text S2. The potential impact of natural variability on AMOC evolution

In the CMIP5 archive, only the first abrupt4×CO_2 ensemble member is long enough to perform our analyses. To examine the robustness of the AMOC index defined in abrupt4×CO_2 experiments using just one ensemble member per model, we quantify the natural variability of the AMOC evolution in longer piControl simulations. For each model, we define "piControl AMOC indices" as follows. First, we calculate the trends of AMOC in each 20-year chunk in a 500-yr piControl simulation, which gives us 25 independent AMOC trends. Then, we take the difference between any 2 AMOC trends from the 25 AMOC trends, which gives us 600 possible changes in AMOC trend (the permutation of choosing 2 from 25 equals 600). These 600 possible changes are piControl AMOC indices, representing changes in AMOC trend resulting from natural variability. The probability distribution of the piControl AMOC indices is close to the normal distribution in all models. Hence, we plot 1 standard deviation of the piControl AMOC indices from each model to compare with the corresponding abrupt4×CO_2 AMOC index (Figure S6). The 1 standard deviation values of the piControl AMOC indices (red bars) are smaller than the abrupt4×CO_2 AMOC indices in most models (black bars) and are unlikely to influence the intermodel spread of abrupt4×CO_2 AMOC indices significantly. The comparison between piControl AMOC indices and abrupt4×CO_2 AMOC indices is a conservative test since the piControl indices are based on the difference between 20-year AMOC trends, while the abrupt4×CO_2 indices are the changes in AMOC trend between the early (Y1-20) and late (Y21-150) periods, which should be less affected by natural variability. Despite potentially overestimating the impact of natural variability, we still find that the abrupt4×CO_2 AMOC index is robust. We conclude that natural variability is unlikely to affect the model spread of AMOC evolution discussed in our manuscript.

Text S3. The dominant mode of inter-model spread of the evolution in global overturning circulation

As discussed in the Results section, we suggest that about half of the uncertainty of ocean circulation evolution across models can be attributed to the AMOC. The following text describes the method and provides additional details.

First, we apply equation (2) with X as the meridional mass streamfunction for the global ocean, which gives us the evolution of the global meridional overturning circulation (GMOC). The GMOC represents the global-scale ocean conveyor belt that connects the Arctic, Atlantic, Indian, and Pacific Ocean via the Southern Ocean (Schmitz Jr, 1995; Talley et al., 2003; Lee et al., 2019), and the GMOC evolution quantifies its slow adjustments to greenhouse gas forcings. Figure S7 shows the multimodel-mean GMOC evolution, which features the strengthening of the AMOC and the weakening of the Southern Ocean circulation. Also, the AMOC strengthening is highly model-dependent (the dots label regions where 1 standard deviation of the GMOC evolution across models exceeds its multimodel-mean magnitude). To investigate the intermodel spread of the global ocean circulation evolution, we apply EOF analysis onto the GMOC evolution across models. The first EOF pattern resembles the structure of the AMOC (Figure S8), suggesting the AMOC evolution dominates the intermodel spread of ocean circulation evolution. Also, the principal component corresponding to the first EOF is well correlated with our AMOC index used in the manuscript (Figure S9), which supports the conclusion that the first EOF mode is related to the AMOC.

Text S4. The contribution of local climate feedback

As discussed in section 3.3, we attribute the intermodel spread of climate feedback evolution to the spread of tropospheric stability evolution. There is an alternative hypothesis, proposed by Armour et al. (2013), suggesting that when assuming time-invariant local feedbacks, the changes in global-mean feedbacks are merely the result of the surface warming pattern evolution accompanied by constant local feedbacks, termed "effective climate feedbacks". Here we evaluate whether the intermodel spread of climate feedback evolution can be explained by the local feedback perspective. Following the method of Ceppi and Gregory (2017), we define the evolution of effective climate feedbacks as follows:

$$\delta\lambda_{\mathrm{eff}} = \lambda_{\mathrm{local}}\delta\mathrm{TAS}.$$

$\delta\lambda_{\mathrm{eff}}$ means the change in effective climate feedback between Yr 1-20 and Yr 21-150 of the abrupt4×CO_2 simulations. λ_{local} is the local climate feedback, defined as the radiative anomalies at each grid point divided by the local surface air temperature anomaly. λ_{local} is assumed to be constant with time. To exclude the rapid adjustments from the calculations, the anomalies are calculated by subtracting the mean of the first 10 years from the mean of the last 20 years of abrupt4×CO_2, as in Ceppi and Gregory (2017). $\delta\mathrm{TAS}$ is the pattern evolution of surface air temperature, using equation (2) in section 2.2.

Comparing the regression slopes of the effective climate feedback evolution ($\Delta\lambda_{\mathrm{eff}}$) against the AMOC index with the regression slopes based on the standard definition of climate feedbacks (section 2.2), most of the climate feedback components show little resemblance between them, with pattern correlations lower than 0.2. The albedo feedback is the only exception, with a pattern correlation of 0.7, indicating that the surface warming pattern evolution itself can explain the relationship between the AMOC index and the albedo feedback, given a constant local albedo feedback. For other feedback components, changes in local feedbacks or non-local effects need to be considered.

Text S5. Variability in piControl simulations

To evaluate if the link between AMOC strength and climate feedbacks proposed in the study can be observed in individual models, we investigate the joint variability in AMOC strength and radiative anomalies in long-term unforced piControl simulations in each model. The run length varies among models but always exceeds 500 years (Table S1). To remove the high-frequency variability, a 5-year low-pass Lanczos filter is applied to all the variables. To isolate the contribution of AMOC variability from the effect of global warming or cooling, we apply multiple linear regression as follows:

$$y = \beta_0 + \beta_1 X_1 + \beta_2 X_2 + \epsilon.$$

The two independent variables X_1 and X_2 are the anomalous AMOC intensity and GMT anomaly, respectively. The dependent variable y can be any of the target fields, for example, radiative anomalies. The least-squares estimate β_1 is the regression coefficient that measures a change in the dependent variable when the anomalous AMOC intensity changes, while holding GMT anomaly fixed, and vice versa for β_2. β_0 is the intercept term. Since X_1, X_2, and y are all anomalies in our case, β_0 equals to zero. ϵ denotes the residual term.

Figures S10a and S10b show that when holding GMT anomaly fixed, most models experience a warmer NH and a cooler SH when the AMOC is stronger. Also, EIS decreases in the NH, which leads to more positive lapse-rate radiative anomalies in most of the NH and more positive shortwave cloud radiative anomalies in the NH mid-latitudes, especially in the North Atlantic, associated with a stronger AMOC (Figure S10). Our results highlight the similar structures between the contribution of the AMOC variation in piControl simulations and the evolving responses due to the varying AMOC index in abrupt4×CO_2 experiments (compare Figure S10 with Figures 3 and 4). This resemblance suggests that in both forced and unforced simulations, the varying AMOC strength controls the surface warming pattern, thereby altering radiative fluxes via changing tropospheric stability.

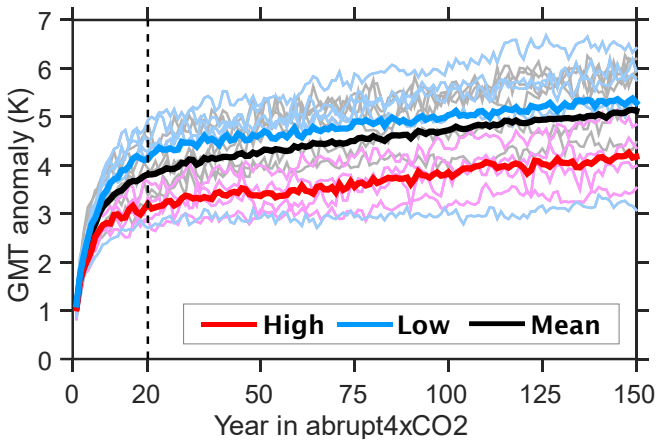

Figure S1. The time evolution of GMT in abrupt4×CO_2 simulations. The black line indicates the multimodel mean, while the thick red (blue) line indicates the high (low) AMOC index composite mean, and the thin red (blue/gray) lines are from individual models with high (low/medium) AMOC index.

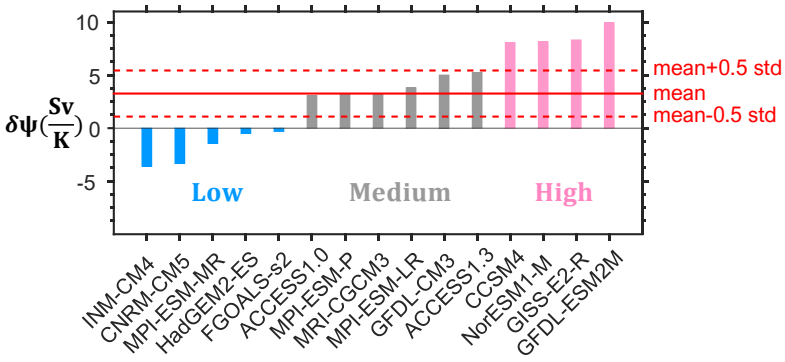

Figure S2. The AMOC index ($\boldsymbol{\delta\Psi}$) in each model. The solid red line indicates the model-mean AMOC index, and the dashed lines indicate the model mean ±0.5 standard deviation (std) across models.

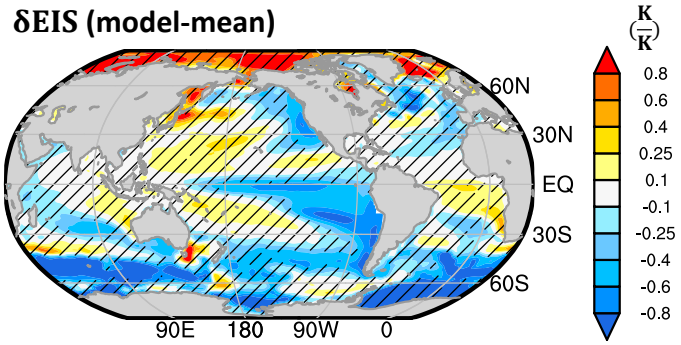

Figure S3. (a) Multimodel-mean pattern evolution of estimated inversion strength (**δEIS**). Hatching indicates that the absolute value of the multimodel mean is smaller than 1 standard deviation of the inter-model spread.

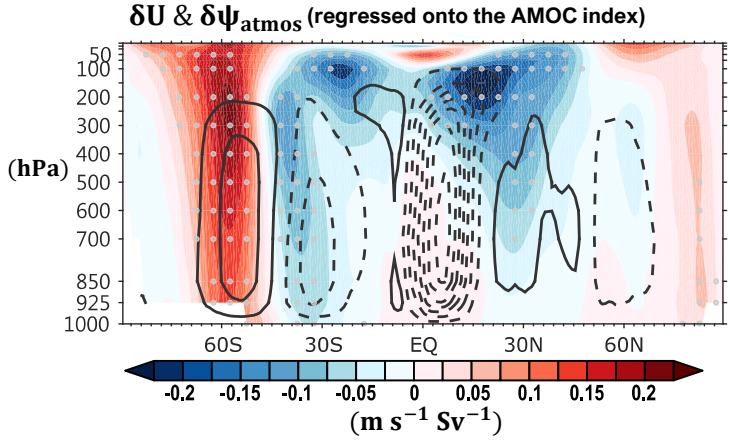

Figure S4. Shading shows the regression slopes of the zonal-mean zonal wind evolution against the AMOC index, with gray stippling denoting the significance at the 95% confidence level. Contours indicate the regression slopes of the atmospheric mass streamfunction evolution against the AMOC index, with clockwise direction in solid contours and counterclockwise direction in dashed contours.

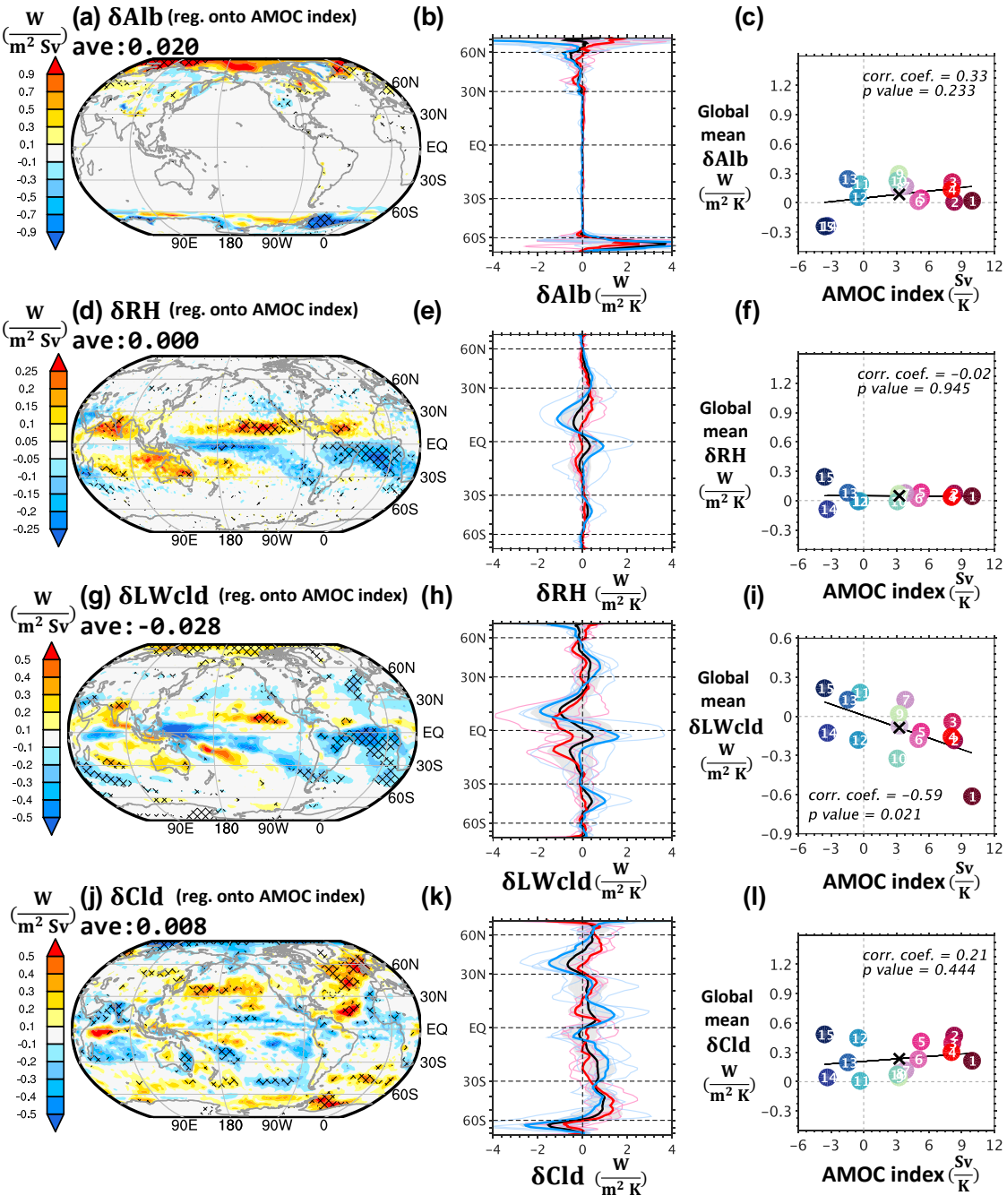

Figure S5. Same as Figure 4, but for (a-c) surface albedo feedback, (d-f) relative humidity feedback, (g-i) longwave cloud feedback, and (j-l) net cloud feedback.

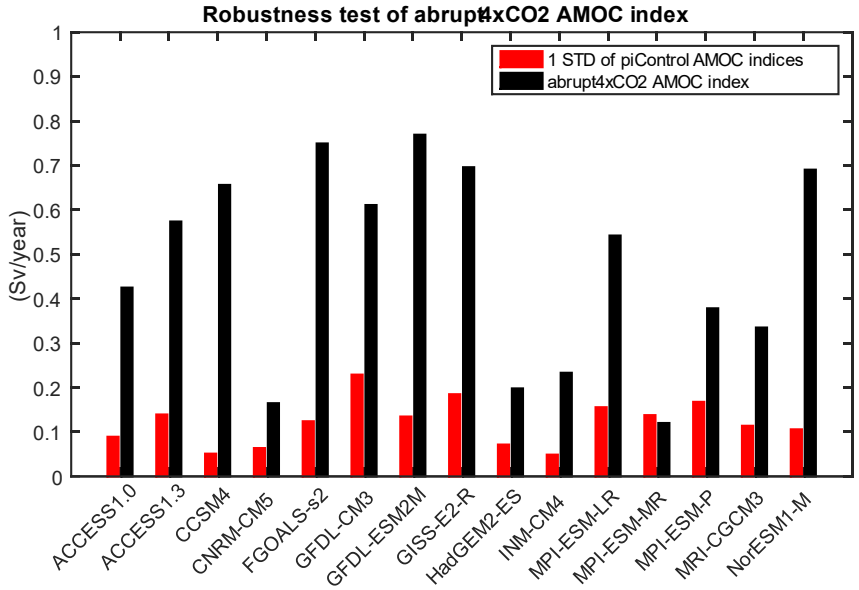

Figure S6. Comparison between piControl AMOC indices (red bars) and abrupt4×CO_2 AMOC indices (black bars) for each CMIP5 model, as defined in Text S2.

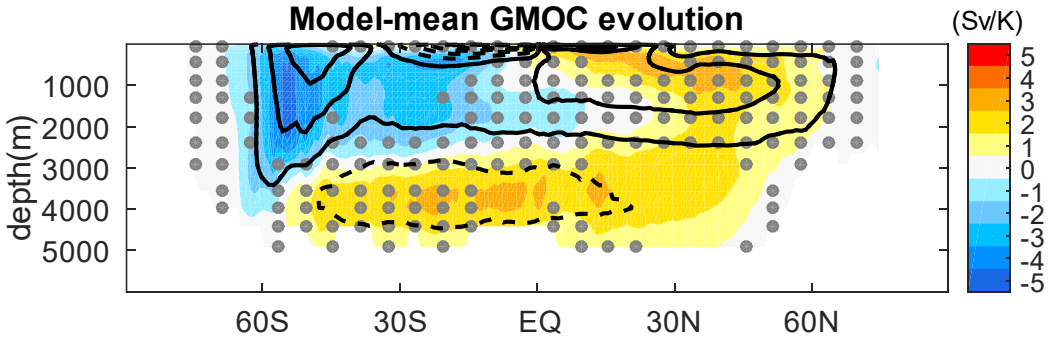

Figure S7. The shading shows the multimodel-mean GMOC evolution (Sv/K). Contours show the GMOC climatology (Sv), with clockwise direction in solid contours and counterclockwise direction in dashed contours. Dots indicate the regions where 1 standard deviation of GMOC evolution across models is larger than its multimodel-mean magnitudes.

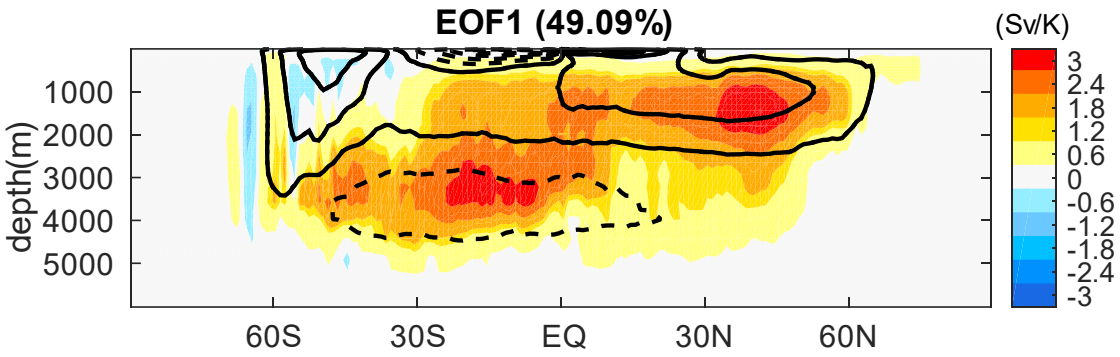

Figure S8. The shading shows the first EOF pattern of the GMOC evolution across models, which explains 49.1% of the total variance. Contours show the GMOC climatology (Sv), with clockwise direction in solid contours and counterclockwise direction in dashed contours.

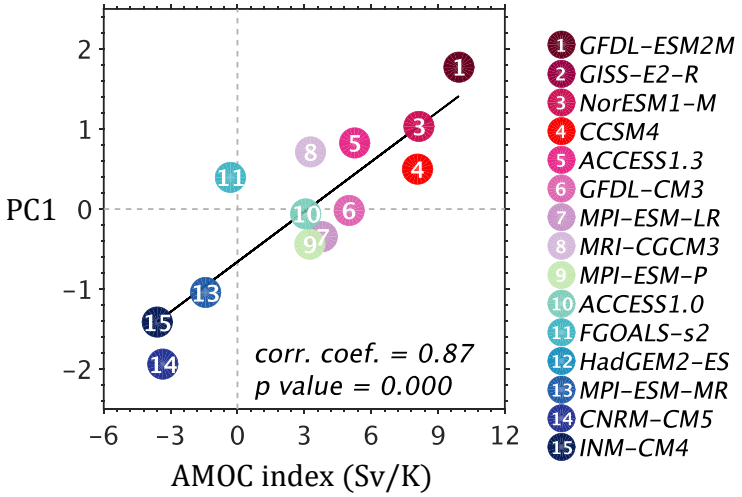

Figure S9. The principal component corresponding to the first EOF of the GMOC evolution (y-axis) versus the AMOC index used in the manuscript (x-axis). The correlation coefficient is 0.87 (Note that models #2 and #12 are missing due to data availability.)

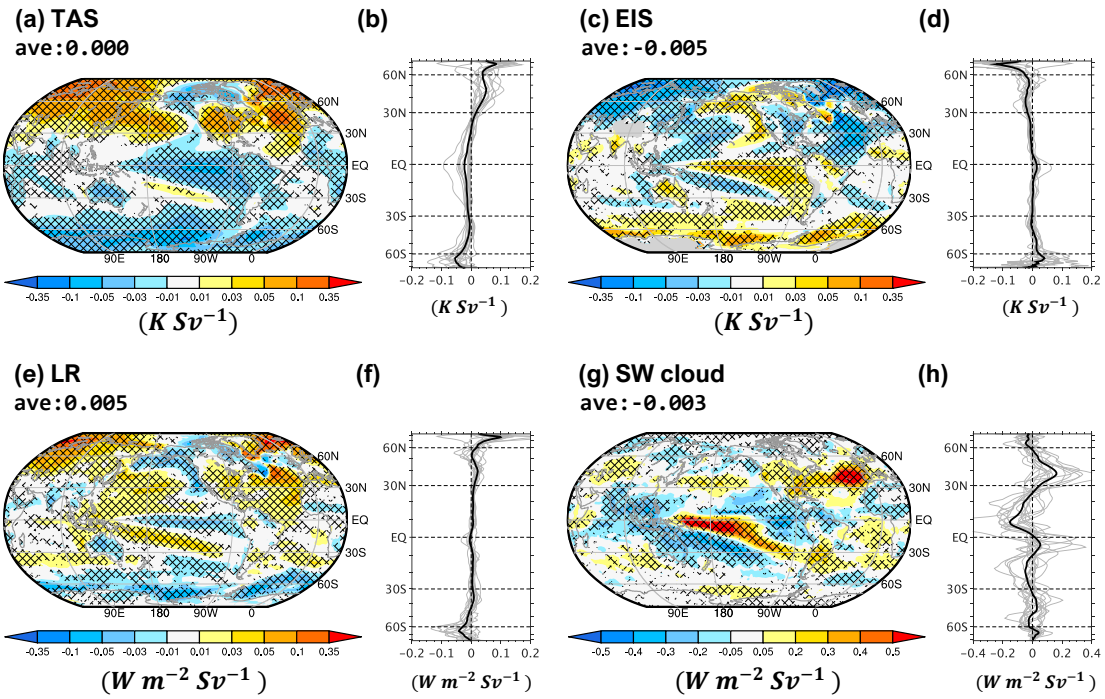

Figure S10. Multimodel-mean regression slopes of 5-year low-pass-filtered (a) surface air temperature, (c) EIS, (e) lapse-rate radiative anomaly, and (g) shortwave cloud radiative anomaly against 5-year low-pass-filtered AMOC strength while holding global-mean surface air temperature anomaly fixed in pre-industrial simulations. Meshing indicates that 10 out of the 15 analyzed models agree on the sign. (b, d, f, h) The black line is the zonal average of (a), (c), (e), and (g), respectively, and light gray lines are the zonal averages of individual models.

Model	Institute (country)	Time periods in piControl	Ψ_{1-20}	Ψ_{21-150}	$\delta\Psi$	PC	$\delta\lambda$
ACCESS1.0	Commonwealth Scientific and Industrial Research Organization/Bureau of Meteorology (Australia)	030001-079912	-2.91	0.16	3.07	0.77	0.51
ACCESS1.3		025001-074912	-4.05	1.21	5.26	0.51	0.67
CCSM4	National Center for Atmospheric Research (USA)	080001-130012	-4.75	3.32	8.08	0.64	0.65
CNRM-CM5	Centre National de Recherches Météorologiques (France)	185001-269912	-1.03	-4.38	-3.35	-1.72	-0.18
FGOALS-s2	Institute of Atmospheric Physics, Chinese Academy of Sciences (China)	185001-235012	-4.24	-4.57	-0.33	-1.71	0.17
GFDL-CM3	Geophysical Fluid Dynamics Laboratory (USA)	000101-050012	-4.82	0.19	5.01	0.01	0.53
GFDL-ESM2M		000101-050012	-5.99	3.95	9.94	0.89	0.23
GISS-E2-R	NASA/ GISS (Goddard Institute for Space Studies) (USA)	333101-363012 398101-453012	-9.41	-1.09	8.33	0.27	1.05
HadGEM2-ES	Met Office Hadley Centre (UK)	185912-243511	-1.26	-1.76	-0.50	0.64	0.47
INM-CM4	Russian Academy of Sciences, Institute of Numerical Mathematics (Russia)	185001-234912	-2.84	-6.44	-3.60	-2.16	0.44
MPI-ESM-LR	Max Planck Institute for Meteorology (Germany)	185001-284912	-3.30	0.50	3.80	0.43	0.42
MPI-ESM-MR		185001-284912	-0.99	-2.43	-1.44	0.08	0.58
MPI-ESM-P		185001-284912	-2.52	0.72	3.25	0.70	0.58
MRI-CGCM3	Meteorological Research Institute (Japan)	185001-284912	-3.51	-0.24	3.27	-0.38	0.48
NorESM1-M	Bjerknes Centre for Climate Research, Norwegian Meteorological Institute (Norway)	185001-284912	-6.67	1.49	8.15	1.04	0.80

Table S1. The list of CMIP5 models used, with the time periods [yyyy-mm] analyzed in the piControl simulations, the regression slopes of AMOC strength anomaly against GMT anomaly in year 1-20 ($\boldsymbol{\Psi_{1-20}}$) and year 21-150 ($\boldsymbol{\Psi_{21-150}}$), the AMOC indices ($\boldsymbol{\delta\Psi}$), the principal components (PC) corresponding to the first EOF, and the global-mean $\boldsymbol{\delta\lambda}$.

	Year 5	*Year 10*	*Year 15*	*Year 25*	*Year 30*	*Year 35*
Year 20	0.85	0.95	0.99	0.99	0.96	0.92

Table S2. The correlation coefficients between AMOC indices that are calculated based on different cutoff years between the fast and slow responses. For example, 0.85 is the correlation coefficient between the AMOC indices based on cutoffs at Year 20 and Year 5.